# Permeability evolution during localized deformation in Bentheim sandstone

Veronika Vajdova
Department of Geosciences, State University of New York at Stony Brook, Stony Brook, New York, USA

Patrick Baud
Institut de Physique du Globe, Ecole et Observatoire des Sciences de la Terre (CNRS/ULP), Strasbourg, France

Teng-fong Wong
Department of Geosciences, State University of New York at Stony Brook, Stony Brook, New York, USA

Received 16 December 2003; revised 29 June 2004; accepted 27 July 2004; published 14 October 2004.

[1] Strain localization in porous sandstones may significantly impact the regional fluid flow. Previous laboratory studies that investigated permeability evolution with deformation concentrated primarily on shear localization and distributed cataclastic flow. Here we focus on compaction bands, a localized mode of deformation characterized by compaction and negligible shear. In this study we used Bentheim sandstone with porosity 23%, where discrete compaction bands have been observed to develop subperpendicular to the maximum principal stress. To investigate coupling between strain localization and permeability, we conducted permeability measurements during triaxial loading at confining pressures ranging from 10 to 350 MPa and microstructural observation on failed samples. Two types of failure were identified: shear localization and compaction localization at low and high effective pressures, respectively. For both failure modes the bulk permeability decreased with deformation. A dramatic decrease of more than one order of magnitude was associated with compaction localization, where permeability reduction occurred over a relatively narrow range of axial strain with the onset of shear-enhanced compaction. Motivated by our microstructural observations, we modeled the permeability reduction of the failed sample as that of a layered medium with significant permeability contrast between the discrete bands and matrix. The model reproduced the experimental observations of permeability evolution during development of discrete compaction bands, with implications for the amount of localized strain and the permeability contrast. Permeability evolution during development of discrete and diffuse compaction bands suggests two different trends with strain, providing guidance for extrapolation of laboratory measurements to field settings. *INDEX TERMS:* 5114 Physical Properties of Rocks: Permeability and porosity; 5112 Physical Properties of Rocks: Microstructure; 5104 Physical Properties of Rocks: Fracture and flow; 8010 Structural Geology: Fractures and faults; *KEYWORDS:* hydraulic permeability, deformation bands, localization

**Citation:** Vajdova, V., P. Baud, and T.-f. Wong (2004), Permeability evolution during localized deformation in Bentheim sandstone, *J. Geophys. Res.*, *109*, B10406, doi:10.1029/2003JB002942.

## 1. Introduction

[2] In the upper crust where the ambient temperature and pressure are relatively low, strain localization commonly develops along planar structures with petrophysical properties that may differ from the host rock. In sedimentary formations, such a localized mode of failure is represented by faults and deformation bands associated with dilatant or compactive volumetric strain that can significantly impact the regional fluid flow [*Caine et al.*, 1996; *Borja and Aydin*, 2004].

[3] Solving problems in geotechnical engineering (such as design of waste repositories) or in petroleum geology (such as prediction of reservoir deformation and fluid flow), hinges on realistic estimation of permeability and its evolution as a function of stress, strain and porosity. Significant hydromechanical coupling occurs during reservoir depletion [*Bouteca et al.*, 2000] and water injection [*Heffer*, 2002]. Hydrocarbon traps and compartments may arise from capillary and hydromechanical seals. Processes that have been proposed for the development of hydromechanical seals include clay smearing, diagenesis and cataclasis [*Knipe*,


0148-0227/04/2003JB002942$09.00

1997]. Laboratory studies play a key role in providing insights into the permeability evolution with rock deformation in two ways. First, they allow direct measurements of permeability on samples from faults and deformation bands [*Antonellini and Aydin*, 1994; *Sternlof et al.*, 2004], and second, they help to establish a relationship between deformation and permeability [e.g., *Wong and Zhu*, 1999; *Keaney et al.*, 1998; *Main et al.*, 2000; *Heiland and Raab*, 2001; *Morris et al.*, 2003].

[4] While most laboratory studies have investigated permeability evolution in relation to shear localization or distributed cataclastic flow, limited attention has been paid to that in relation to compaction localization. Here we focus on compaction bands, a mode of localized failure characterized by compactive cataclasis with negligible shear first described by *Mollema and Antonellini* [1996] in aeolian porous sandstone. Similar structures have since been documented in laboratory experiments [*Olsson*, 1999; *Olsson and Holcomb*, 2000; *Klein et al.*, 2001; *Wong et al.*, 2001] and predicted by theoretical analyses [*Olsson*, 1999; *Issen and Rudnicki*, 2000, 2001]. Recently, *Baud et al.* [2004] investigated in the laboratory five sandstones with porosities ranging from 13% to 24%, and they identified two end members of this failure mode. On one hand, discrete compaction bands can develop in relatively porous sandstone. On the other hand, high-angle shear bands can develop in relatively compact sandstone. In sandstone with intermediate porosity a hybrid mode manifested by diffuse compaction bands was also observed. Geometry of both discrete and diffuse compaction bands is characterized by their orientation perpendicular to the maximum principal stress, but while the ''discrete'' compaction bands have a thickness of only few grains and are rather numerous, the ''diffuse'' compaction bands are significantly thicker and fewer in number. Some of the best examples of discrete and diffused compaction bands have been observed in Bentheim sandstone [*Klein et al.*, 2001; *Wong et al.*, 2001; *Baud et al.*, 2004] and Castlegate sandstone [*Olsson*, 1999; *Olsson and Holcomb*, 2000; *DiGiovanni et al.*, 2000], respectively.

[5] It is likely that such localized cataclastic structures will act as hydraulic barriers, but there are a paucity of field and laboratory data on their hydromechanical characteristics. During the development of diffuse compaction bands, *Holcomb and Olsson* [2003] measured the permeability of Castlegate sandstone at effective pressure of 35 MPa, and observed a decrease in permeability by two orders of magnitude. Their data represent the first measurements of permeability evolution during compaction localization. A primary objective of this study is to conduct similar measurements in Bentheim sandstone during the development of discrete compaction bands. We selected effective pressures in the range from 10 to 350 MPa to map out the permeability evolution as the failure mode of Bentheim sandstone undergoes a transition from shear localization to formation of discrete compaction bands. Microstructure observations were also performed to elucidate the spatial distribution of damage in the failed samples. Specifically, this study was undertaken to address several related questions. Are there fundamental differences in permeability evolution in relation to shear localization and compaction localization? By how much does the permeability decrease while the sandstone compacts and develops discrete compaction bands? To what extent is the permeability evolution similar to that in sandstone that fails by the development of diffuse compaction bands? What are the microstructural bases for the percolative behavior in relation to compaction localization?

## 2. Rock Material and Experimental Procedure

[6] Our sandstone block is from the Gildehausen quarry, near the village of Bentheim, Germany. The modal composition was reported by *Klein and Reuschlé* [2003] to be quartz (95%), kaolinite (3%) and microcline (2%). The grain diameter ranges between 0.1 and 0.3 mm [*Louis et al.*, 2003]. (It should be noted that there is a typographical error in the work of *Louis et al.* [2003, Table 1] where the column title ''Grain radius'' should read ''Grain diameter'' (L. Louis, personal communication, 2003)). Our samples were from the same block used by *Vajdova and Wong* [2003]. They were cored perpendicular to bedding and ground to a cylindrical shape, with diameter of 18.4 mm and length 38.1 mm. The samples were first oven dried in a vacuum for 24 hours, then saturated with distilled water. The interconnected porosity was found to be between 22 and 23 % with a mean value of 22.3%, by comparing the dry and water-saturated masses. Each sample was jacketed in a thin copper foil and placed between two steel end-plugs, each of which has a concentric hole for fluid connection to the upstream or downstream pore pressure system. Channels were carved into the contact face of the end-plugs to help distribute the fluid evenly to the face of the sample. Heat shrinkable polyolefine tubing was used to separate the sample from the confining pressure medium (kerosene).

[7] Saturated samples were deformed at room temperature in the conventional triaxial configuration, with principal stresses $\sigma_1 \geq \sigma_2 = \sigma_3$. All experiments were conducted at a nominal pore pressure $P_p$ of 10 MPa using distilled water as the pore fluid, and confining pressures $P_c = \sigma_3$ in the range from 13 to 360 MPa. The axial and lateral stresses ($\sigma_1$, $\sigma_3$) were raised first to 3 MPa while pore pressure was maintained atmospheric. As the axial and lateral stresses were increased by equal increments (to maintain hydrostatic conditions) to 13 MPa, the pore pressure was raised simultaneously to 10 MPa to keep constant effective pressure ($P_c - P_p$) of 3 MPa. The axial and lateral stresses were then raised to a desired value of confining pressure while pore pressure was maintained at its nominal value of 10 MPa. Keeping the lateral stress constant, the axial stress was increased to generate a differential stress ($\sigma_1 - \sigma_3$). The axial load was measured with an external load cell, and the displacement was measured outside the pressure vessel with a displacement transducer (DCDT) mounted between the moving piston and the fixed upper platen. Axial strain was calculated from the displacement corrected for the machine deformation normalized by the initial sample length. During loading, the axial displacement was servo-controlled at a fixed rate corresponding to a nominal strain rate of $1.0 \times 10^{-5}$ s$^{-1}$. Adjustment of a pore pressure generator kept the pore pressure constant, and the pore volume change was recorded by monitoring the piston displacement of the pressure generator with a displacement

transducer. The porosity change was then calculated as the pore volume change divided by the initial bulk volume of the sample assuming that the bulk volume was not affected by the effective pressure increase from 0 to 3 MPa at the start of the experiment.

[8] The samples were loaded to different stages of deformation and the in situ permeability was measured for hydraulic flow in the axial ($\sigma_1$) direction after stresses were equilibrated in the samples. We used the permeability setup of *Zhu and Wong* [1997] with the modification that instead of a pipette, an electronic balance connected directly to a personal computer was used to measure the flux through the sample. In our experiments the permeability never dropped below $10^{-16}$ m$^2$, and therefore hydraulic steady state and thermal stability could readily be attained making it possible to use the steady state flow method for measurement. While the upstream pore pressure was kept constant at $P_p$ = 10 MPa, the downstream pressure was reduced by a small constant increment of $\Delta P_p$, forcing the fluid to flow from upstream to downstream through the sample. The pore pressure difference $\Delta P_p$ was measured with a differential pressure transducer. The experimental error of permeability measurement was less than 15% in most experiments. In calculating the values of permeability, temperature variations of water viscosity and density have been accounted for. Altogether nine experiments were conducted at seven different confining pressures to axial strains ranging up to 13%.

## 3. Experimental Results

[9] Figure 1a shows differential stress versus axial strain curves for selected experiments. The porosity as a function of effective mean stress ($[\sigma_1 + \sigma_2 + \sigma_3]/3 - P_p$) is shown at Figure 1b, at stress states corresponding to the permeability measurements. Following *Wong et al.* [1997] the critical stresses at the onset of dilatancy and shear-enhanced compaction are denoted by $C'$ and $C^*$, respectively.

[10] The two samples loaded triaxially at effective pressures of 10 and 30 MPa failed by the development of shear bands at angles of 25° and 45°, respectively, to the $\sigma_1$ direction. The stress-strain curves show a peak stress followed by strain softening (Figure 1a). This failure mode will be referred to as "shear localization." While dilatancy was observed in the pre- and post-failure stages of the experiment at an effective pressure of 10 MPa, negligible porosity change was observed during the experiments at 30 MPa.

[11] At effective pressures of 120, 250, 300 and 350 MPa the differential stress increased until it reached a plateau punctuated by episodic stress drops (with amplitudes <10 MPa), after which the samples would undergo a second stage of strain hardening (Figure 1a). Compaction was observed in all these stages of deformation (Figure 1b). Microstructural observations revealed discrete compaction bands sub-perpendicular to $\sigma_1$. This failure mode will be referred to as "compaction localization."

[12] The episodic stress drops at the plateau should not be mistaken with those of larger magnitude related to stress relaxation that occurred while the loading piston was stopped to allow the sample assembly to attain hydraulic and thermal equilibrium before a permeability measurement was conducted. Figure 1c depicts these two features of the stress-strain curve for the experiment at effective pressure of 350 MPa. During the hold period the differential stress drops rapidly at first but reaches a constant value with time, at which point the permeability measurement is initiated. Since the axial stress was measured with an external load cell, o-ring friction of the loading piston (which we estimated to be up to 30 MPa in some of the high-pressure experiments) can contribute significantly to the apparent stress relaxation.

[13] This methodology (that was previously adopted by *Zoback and Byerlee* [1975], *Fischer and Paterson* [1992], and *Zhu and Wong* [1997]) ensures that specific storage of a sample does not fluctuate significantly during a permeability measurement. However, it has the shortcoming in that permeability can only be measured at the relaxed state but not at stress states associated with continuous loading. The alternative is to monitor the difference in up- and downstream pressure with a constant flux of fluid percolating through a sample that is deformed continuously at a given rate [e.g., *Main et al.*, 2000; *Heiland and Raab*, 2001; *Holcomb and Olsson*, 2003]. The permeability can then be taken as inversely proportional to the pressure difference if storage remains constant so that the flow behavior is steady state. However, the development of dilatancy or shear-enhanced compaction may occur so rapidly that the resultant changes in storage induce transient flow and consequently the steady state assumption no longer applies. This problem is particularly acute during development of strain localization. *Grueschow et al.* [2003] theoretically analyzed how the suction due to a dilating shear band results in an apparent permeability enhancement that is solely an artifact of a violation of the steady-state assumption.

[14] Permeability during hydrostatic compaction is found in the range from $4 \times 10^{-13}$ to $2 \times 10^{-14}$ m$^2$. Under triaxial compression permeability as a function of axial strain (Figure 2a) shows a decrease by two orders of magnitude in samples that failed by compaction localization, and one order of magnitude in samples that failed by shear localization. Figure 2b shows permeability as a function of effective mean stress. Under hydrostatic loading the permeability reduction follows approximately linear trend in a log-linear plot which is consistent with data for other porous sandstones [*David et al.*, 1994]. For samples that failed by compaction localization significant permeability reduction was observed with the onset of shear-enhanced compaction $C^*$.

[15] The permeability and mechanical data are compiled in Table 1. In Figures 1 and 2 we did not include the experiment conducted at an effective pressure of 200 MPa. In this experiment dilatancy and permeability enhancement occurred as soon as differential stress was applied, although the reverse was expected. We suspect that at the beginning of this experiment, the loading had deviated from hydrostatic and consequently induced damage in the sample. The sample that failed at effective pressure of 120 MPa was buckled, probably due to slight misalignment in the piston column. The asymmetric geometry may result in the relatively large fluctuation in permeability for this sample (Figure 2). These two experiments are excluded from our subsequent analysis of permeability evolution.

[16] At effective pressure of 250 MPa, permeability measurements were conducted on three samples deformed

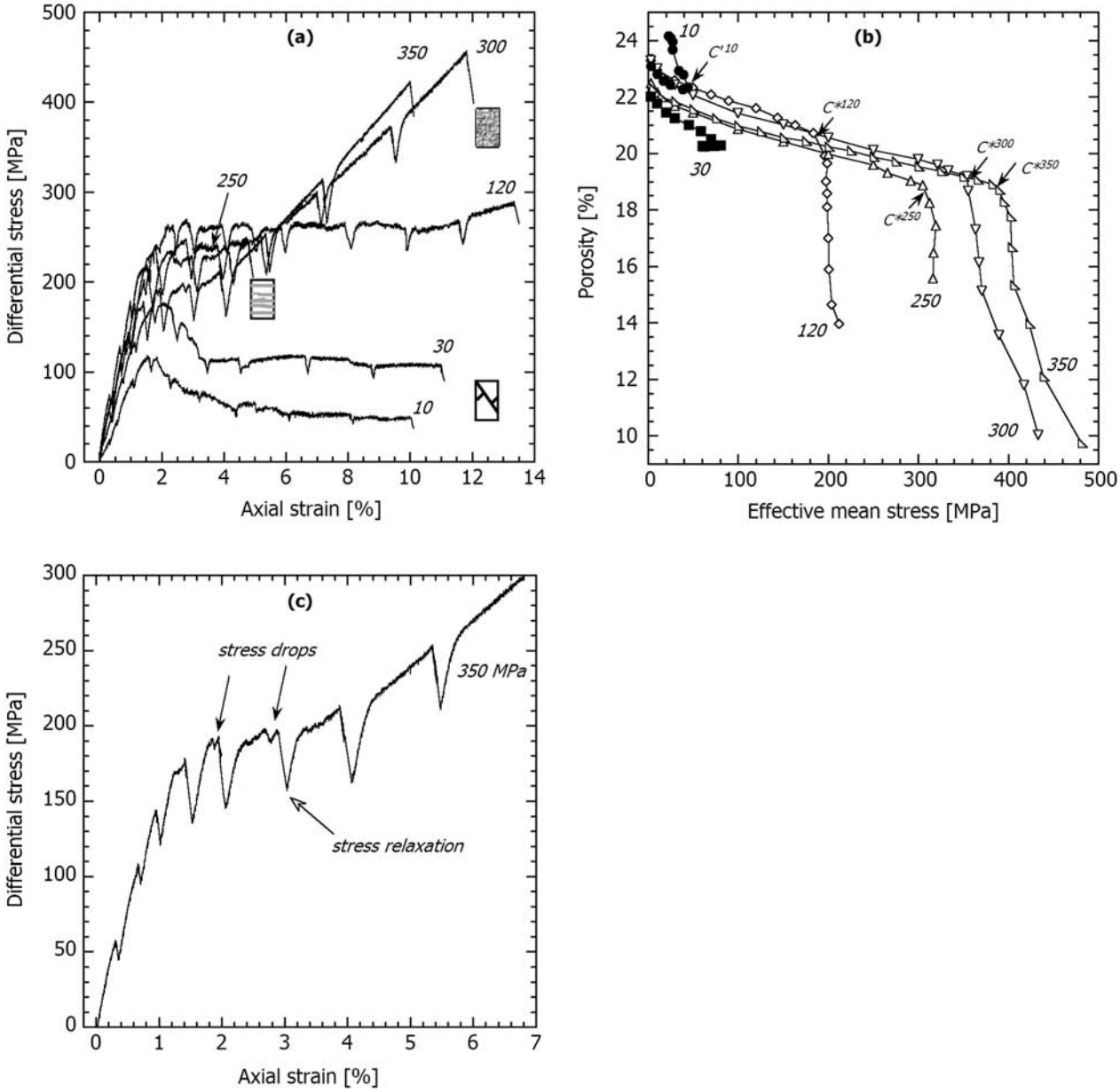


**Figure 1.** (a) Differential stress versus axial strain for selected experiments. Schematic diagrams are also inserted to indicate failure modes and the damage accumulated at the given axial strain. (b) Porosity evolution as a function of effective mean stress for selected experiments. Arrows mark the onset of shear-induced dilatancy $C'$ and shear-enhanced compaction $C^*$. (c) Detail of the curve of differential stress versus axial strain for experiment at effective pressure of 350 MPa, demonstrating the difference between stress drops due to the formation of compaction bands and stress relaxation due to the stop of the loading piston. (Effective pressures are indicated for each experiment.)

to different amounts of axial strain. As shown in Figure 3, the permeability as a function of axial strain follows similar trends, but its magnitude differs by as much as a factor of 5, an indication of the variability among samples.

## 4. Microstructural Observations

[17] After the triaxial experiments at effective pressures of 10, 120, 200, 250 and 300 MPa samples were unloaded and thin sections were prepared for microstructure observations by cutting the samples in the axial direction. All microstructure observations were made using an optical microscope with transmitted or reflected light. A micrograph of undeformed Bentheim sandstone is presented at Figure 4 for a reference.

### 4.1. Development of Shear Localization

[18] *Klein et al.* [2001] and *Klein and Reuschlé* [2003] have studied the failure of dry Bentheim sandstone by shear localization. Our mechanical data and microstructural obser-

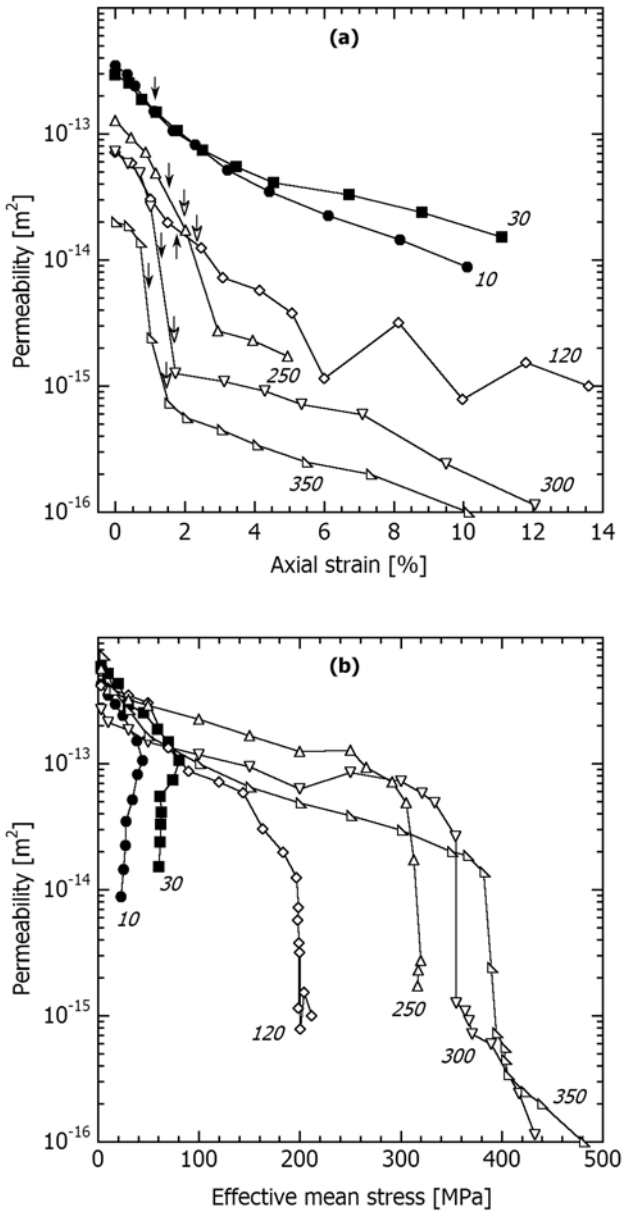


**Figure 2.** (a) Permeability as a function of axial strain during triaxial loading, selected experiments. Solid arrows mark the onset of inelastic deformation (shear-induced dilatancy or shear-enhanced compaction). Open arrows mark the initiation of compaction band formation $C_{cb}$ inferred in section 5.3. (b) Permeability as a function of effective mean stress during hydrostatic and triaxial loading, selected experiments. (Effective pressures are indicated for each experiment.)

vations on saturated samples are qualitatively similar, but the pressure range in which dilatant faulting was observed in this study is lower than that for the dry samples. While *Klein and Reuschlé* [2003] observed appreciable dilatancy in dry samples deformed at confining pressures up to 35 MPa, negligible dilatancy was observed in our saturated sample at effective pressure of 30 MPa. The porosity evolution of our sample is akin to that in a dry sample deformed by *Klein et al.* [2001] at the more elevated pressure of 60 MPa. These differences are possibly due to the presence of water and relaxation of stress that occurred due to the permeability measurements in this study [*Baud et al.*, 2000].

[19] *Klein and Reuschlé* [2003] observed a single shear band in samples that failed at pressures up to 35 MPa at axial strains less than 1.5%. In our samples deformed to significantly higher strains, brittle faulting at effective pressures of 10 and 30 MPa is characterized by development of conjugate shear bands with one major shear zone and several minor shears. The major shear zones were oriented toward $\sigma_1$ at angles of 25° and 45°, respectively. Thin-section examination of the sample deformed at 10 MPa of effective mean stress reveals the localization of shear in a narrow zone (Figure 5a) with grain size reduced at least by one order of magnitude (down to ~5 μm). There is a sharp transition between the fine-grained shear zone and the surrounding damage zone characterized by axial dilatant fractures that had extended from the shear zone to a distance of about four grain sizes. At the intersection with a conjugate shear the main shear zone was observed to widen with deformation accommodated by relative particle motion, moderate grain size reduction and apparent dilation (Figure 5b). Away from the shear zones damage in the form of isolated intragranular cracks can be observed.

### 4.2. Development of Compaction Localization

[20] *Wong et al.* [2001] and *Baud et al.* [2004] have described the compactive failure of dry Bentheim sandstone. *Baud et al.* [2004] observed that compaction bands initiated in short segments near either end of a sample with the implication that the compaction bands have possibly been triggered by the local stress heterogeneity due to interface constraints. With increasing axial strain the bands cut through the cross-section of the sample at an angle ~90° to the direction of $\sigma_1$. As cumulative number of bands increased, they clustered to constitute two parallel arrays that spread toward the center of the sample. The bands appeared tortuous on the grain scale, were about 0.5 mm wide and often intersected each other. Within a compaction band the grains had been crushed to very small fragments so that it appeared as relatively dark region of intense comminution visible in the thin-section by unaided eye. Outside the bands, few cracks were observed and the damage was negligible beyond a distance of about two or three grains.

[21] Our samples deformed in water-saturated conditions show a similar microstructure. Figure 6a shows the thin-section of a sample triaxially deformed at an effective pressure of 300 MPa to an axial strain of 4.3% (sample B16, Table 2), without stopping the piston for permeability measurements. For comparison we show in Figure 6b the thin-section for a sample loaded at the same effective pressure with stopping for permeability measurements (sample B33, Table 1) that attained maximum strain of 12%. The latter sample has significantly more compaction bands. The dark lines correspond to areas of grain crushing while the relatively undamaged material appears light. It can be seen that the deformation is localized in compaction bands oriented sub-perpendicular to the direction of $\sigma_1$ in the less strained sample. In the highly strained sample, numerous compaction bands become intertwined with one

**Table 1.** Mechanical and Permeability Data for Hydrostatic and Triaxial Compression Experiments on Bentheim Sandstone

| Effective Pressure $P_c - P_p$, MPa | Differential Stress $\sigma_1 - \sigma_3$, MPa | Porosity, % | Axial Strain, % | Permeability, $\times 10^{-15}$ m$^2$ |
|---|---|---|---|---|
| | | *B41* | | |
| 3.0 | 0.0 | 23.1 | | 429.73 |
| 10.0 | 0.0 | 22.8 | 0.00 | 351.10 |
| 10.0 | 21.4 | 22.6 | 0.33 | 295.92 |
| 10.0 | 42.6 | 22.4 | 0.57 | 242.28 |
| 10.0 | 82.7 | 22.3 | 1.10 | 151.26 |
| 10.0 | 101.1 | 22.3 | 1.65 | 105.72 |
| 10.0 | 84.1 | 22.8 | 2.29 | 82.50 |
| 10.0 | 67.4 | 22.9 | 3.21 | 51.60 |
| 10.0 | 52.4 | 23.7 | 4.41 | 34.96 |
| 10.0 | 48.4 | 24.0 | 6.12 | 22.61 |
| 10.0 | 44.8 | 24.1 | 8.17 | 14.55 |
| 10.0 | 38.2 | 24.1 | 10.11 | 8.81 |
| | | *B67* | | |
| 3.0 | 0.0 | 22.0 | | 584.50 |
| 10.0 | 0.0 | 21.8 | | 519.70 |
| 20.0 | 0.0 | 21.5 | | 431.00 |
| 30.0 | 0.0 | 21.2 | 0.00 | 293.63 |
| 30.0 | 45.8 | 21.0 | 0.39 | 253.57 |
| 30.0 | 88.3 | 20.8 | 0.75 | 186.65 |
| 30.0 | 122.1 | 20.4 | 1.17 | 149.25 |
| 30.0 | 153.9 | 20.2 | 1.79 | 105.60 |
| 30.0 | 133.6 | 20.1 | 2.50 | 74.51 |
| 30.0 | 97.9 | 20.1 | 3.47 | 54.99 |
| 30.0 | 100.0 | 20.1 | 4.54 | 40.88 |
| 30.0 | 97.0 | 20.2 | 6.71 | 33.00 |
| 30.0 | 92.9 | 20.2 | 8.82 | 23.82 |
| 30.0 | 90.0 | 20.3 | 11.10 | 15.21 |
| | | *B35* | | |
| 3.0 | 0.0 | 23.3 | | 417.22 |
| 10.0 | 0.0 | 23.0 | | 396.57 |
| 30.0 | 0.0 | 22.6 | | 347.24 |
| 50.0 | 0.0 | 22.3 | | 304.37 |
| 70.0 | 0.0 | 22.1 | | 133.92 |
| 90.0 | 0.0 | 21.9 | | 86.84 |
| 120.0 | 0.0 | 21.6 | 0.00 | 71.76 |
| 120.0 | 69.8 | 21.3 | 0.46 | 58.75 |
| 120.0 | 128.5 | 21.0 | 0.97 | 30.27 |
| 120.0 | 191.2 | 20.7 | 1.46 | 19.74 |
| 120.0 | 229.5 | 19.9 | 2.43 | 12.54 |
| 120.0 | 235.6 | 19.6 | 3.03 | 7.28 |
| 120.0 | 233.8 | 19.0 | 4.09 | 5.72 |
| 120.0 | 237.4 | 18.6 | 5.02 | 3.79 |
| 120.0 | 236.8 | 18.1 | 5.95 | 1.15 |
| 120.0 | 237.6 | 17.0 | 8.10 | 3.17 |
| 120.0 | 237.3 | 15.9 | 9.88 | 0.79 |
| 120.0 | 243.5 | 14.6 | 11.69 | 1.53 |
| 120.0 | 264.4 | 14.0 | 13.51 | 1.00 |
| | | *B34* | | |
| 3.0 | 0.0 | 23.2 | | 125.02 |
| 10.0 | 0.0 | 23.1 | | 112.21 |
| 30.0 | 0.0 | 22.5 | | 76.55 |
| 50.0 | 0.0 | 22.3 | | 61.94 |
| 100.0 | 0.0 | 21.7 | | 39.70 |
| 150.0 | 0.0 | 21.2 | | 21.38 |
| 200.0 | 0.0 | 20.8 | 0.00 | 12.75 |
| 200.0 | 79.1 | 20.9 | 0.60 | 81.25 |
| 200.0 | 113.1 | 20.8 | 0.81 | 76.47 |
| 200.0 | 164.5 | 20.5 | 1.24 | 62.27 |
| 200.0 | 211.5 | 19.8 | 2.11 | 51.03 |
| 200.0 | 196.4 | 18.9 | 3.28 | 12.29 |
| 200.0 | 204.5 | 18.3 | 4.16 | 5.05 |
| 200.0 | 181.2 | 17.6 | 5.17 | 7.28 |
| 200.0 | 201.5 | 17.0 | 6.12 | 4.15 |
| 200.0 | 201.5 | 15.7 | 8.10 | 3.06 |
| 200.0 | 249.7 | 14.4 | 9.93 | 1.57 |
| 200.0 | 279.6 | 13.3 | 11.93 | 0.64 |

**Table 1.** (continued)

| Effective Pressure $P_c - P_p$, MPa | Differential Stress $\sigma_1 - \sigma_3$, MPa | Porosity, % | Axial Strain, % | Permeability, $\times 10^{-15}$ m$^2$ |
|---|---|---|---|---|
| | | *B38* | | |
| 3.0 | 0.0 | 22.5 | | 567.53 |
| 10.0 | 0.0 | 22.2 | | 385.73 |
| 30.0 | 0.0 | 21.7 | | 320.68 |
| 50.0 | 0.0 | 21.4 | | 289.53 |
| 100.0 | 0.0 | 20.9 | | 225.10 |
| 150.0 | 0.0 | 20.4 | | 165.61 |
| 200.0 | 0.0 | 20.0 | | 125.02 |
| 250.0 | 0.0 | 19.6 | 0.00 | 127.09 |
| 250.0 | 52.8 | 19.3 | 0.45 | 93.39 |
| 250.0 | 122.4 | 19.0 | 0.86 | 71.49 |
| 250.0 | 163.1 | 18.9 | 1.16 | 48.65 |
| 250.0 | 189.0 | 18.3 | 2.02 | 17.25 |
| 250.0 | 209.1 | 17.4 | 2.94 | 2.75 |
| 250.0 | 203.0 | 16.5 | 3.94 | 2.31 |
| 250.0 | 205.1 | 15.6 | 4.95 | 1.72 |
| | | *B42* | | |
| 3.0 | 0.0 | 22.8 | | 426.51 |
| 10.0 | 0.0 | 22.6 | | 385.46 |
| 30.0 | 0.0 | 22.0 | | 314.89 |
| 50.0 | 0.0 | 21.7 | | 131.03 |
| 100.0 | 0.0 | 21.1 | | 65.86 |
| 150.0 | 0.0 | 20.6 | | 45.50 |
| 200.0 | 0.0 | 20.2 | | 31.39 |
| 250.0 | 0.0 | 19.8 | 0.00 | 27.72 |
| 250.0 | 56.7 | 19.6 | 0.38 | 13.91 |
| 250.0 | 109.8 | 19.4 | 0.75 | 9.42 |
| 250.0 | 151.7 | 19.2 | 1.13 | 7.30 |
| 250.0 | 194.9 | 18.7 | 1.81 | 3.17 |
| | | *B66* | | |
| 5.0 | 0.0 | 22.1 | | 502.29 |
| 15.0 | 0.0 | 22.0 | | 262.17 |
| 200.0 | 0.0 | 19.6 | | 110.76 |
| 250.0 | 0.0 | 19.2 | 0.00 | 67.49 |
| 250.0 | 57.4 | 18.8 | 0.41 | 35.24 |
| 250.0 | 117.5 | 18.6 | 0.84 | 26.59 |
| 250.0 | 163.2 | 18.3 | 1.17 | 14.84 |
| 250.0 | 193.5 | 17.9 | 1.73 | 9.74 |
| 250.0 | 192.2 | 16.7 | 2.83 | 1.00 |
| | | *B33* | | |
| 3.0 | 0.0 | 23.3 | | 268.91 |
| 10.0 | 0.0 | 23.0 | | 213.13 |
| 30.0 | 0.0 | 22.4 | | 183.91 |
| 50.0 | 0.0 | 22.1 | | 148.29 |
| 100.0 | 0.0 | 21.4 | | 117.55 |
| 150.0 | 0.0 | 21.0 | | 94.25 |
| 200.0 | 0.0 | 20.6 | | 63.33 |
| 250.0 | 0.0 | 20.1 | | 85.57 |
| 300.0 | 0.0 | 19.8 | 0.00 | 72.55 |
| 300.0 | 62.1 | 19.6 | 0.35 | 58.19 |
| 300.0 | 105.4 | 19.4 | 0.70 | 48.97 |
| 300.0 | 161.0 | 19.2 | 1.02 | 26.50 |
| 300.0 | 168.3 | 18.7 | 1.72 | 1.26 |
| 300.0 | 190.4 | 17.3 | 3.12 | 1.09 |
| 300.0 | 200.6 | 16.1 | 4.29 | 0.92 |
| 300.0 | 211.1 | 15.1 | 5.35 | 0.71 |
| 300.0 | 263.5 | 13.6 | 7.10 | 0.59 |
| 300.0 | 339.8 | 11.8 | 9.51 | 0.24 |
| 300.0 | 398.6 | 10.0 | 12.05 | 0.11 |
| | | *B65* | | |
| 5.0 | 0.0 | 22.3 | | 724.17 |
| 15.0 | 0.0 | 22.0 | | 384.19 |
| 30.0 | 0.0 | 21.8 | | 267.70 |
| 50.0 | 0.0 | 21.6 | | 167.09 |
| 100.0 | 0.0 | 21.0 | | 99.93 |
| 150.0 | 0.0 | 20.6 | | 65.09 |
| 200.0 | 0.0 | 20.2 | | 49.04 |
| 250.0 | 0.0 | 19.9 | | 38.99 |

**Table 1.** (continued)

| Effective Pressure $P_c - P_p$, MPa | Differential Stress $\sigma_1 - \sigma_3$, MPa | Porosity, % | Axial Strain, % | Permeability, $\times 10^{-15}$ m$^2$ |
|---|---|---|---|---|
| 300.0 | 0.0 | 19.5 | | 29.66 |
| 350.0 | 0.0 | 19.2 | 0.00 | 19.97 |
| 350.0 | 44.5 | 19.1 | 0.35 | 18.78 |
| 350.0 | 94.8 | 18.9 | 0.71 | 13.92 |
| 350.0 | 120.8 | 18.7 | 1.02 | 2.40 |
| 350.0 | 135.5 | 18.3 | 1.53 | 0.73 |
| 350.0 | 154.4 | 17.8 | 2.03 | 0.56 |
| 350.0 | 156.8 | 16.7 | 3.04 | 0.45 |
| 350.0 | 166.1 | 15.3 | 4.06 | 0.34 |
| 350.0 | 213.1 | 14.0 | 5.48 | 0.25 |
| 350.0 | 265.3 | 12.1 | 7.31 | 0.20 |
| 350.0 | 383.7 | 9.7 | 10.13 | 0.10 |

another. Figure 6c shows a close-up view of grain crushing in the sample B33 with small islands of unfractured grains enclosed by intensely comminuted grains.

[22] Three duplicate experiments at effective pressure of 250 MPa were performed to investigate the microstructure of compaction localization as a function of strain and its effect on permeability. The microstructure at the different stages of deformation is shown in Figure 3. At the onset of shear-enhanced compaction $C^*$ two short segments of compaction bands can be recognized in B42 (axial strain 1.8%), but none of them cut through the entire cross-section of the sample. At slightly higher axial strain of 2.8% two compaction bands clearly cut through the entire thin-section of B66, accompanied by significant permeability reduction. At an axial strain of 5% approximately 11 bands were recognized in B38, accompanied by a more gradual reduction of permeability.

[23] Prior to the formation of a compaction band, intragranular cracking and clusters of crushed grains are observed in Bentheim sandstone as documented in Figure 7a of the sample B42 loaded to just beyond $C^*$. Similar damage was also observed in sample B66 in regions outside of the compaction bands. It is likely that the permeability evolution will be affected by the damage distributed outside the compaction bands as well as by the geometric attributes of the compaction bands (such as spacing, thickness, tortuosity and continuity of the band as a planar structure). Figure 7b shows a tortuous part of a compaction band in B66 associated with intense grain crushing.

### 4.3. Estimation of the Number of Compaction Bands as a Function of Strain

[24] To correlate the permeability and microstructure evolutions, it is necessary to establish the connection between the cumulative development of discrete compaction bands and axial strain. This requires the quantitative characterization of the number $n$ of discrete compaction bands in samples deformed to different amounts of strain. Since we have only a limited number of samples in this study we decided to include samples of Bentheim sandstone deformed by *Wong et al.* [2001] and *Baud et al.* [2004] under dry conditions at effective pressures of 120, 180 and 300 MPa (Table 2).

[25] It is difficult to uniquely determine the number of discrete compaction bands in Bentheim sandstone because of their somewhat tortuous character and tendency to merge and cross-cut one another. Our approach was to set up an array of three test-lines through every thin-section in the axial direction (two near the sides and one in the middle) and count the number of intersections of the compaction bands with each test-line. The arithmetic mean $n$ of these three values is reported in Table 2. Since the microstructural observations show that the compaction bands do not develop until after the onset of shear-enhanced compaction, one expects the cumulative development of such bands to be related to the plastic strain defined by $\varepsilon_p = \varepsilon_{ax} - \varepsilon^* - (Q - Q^*)/E$, where $\varepsilon_{ax}$ is the axial strain at a point beyond the onset of shear-enhanced compaction and $\varepsilon^*$ is that at the point of onset $C^*$. The differential stresses at the two points are denoted by $Q$ and $Q^*$, and if the Young's modulus is denoted by $E$ then the last term represents the elastic strain that has accumulated beyond $C^*$. The Young's modulus was

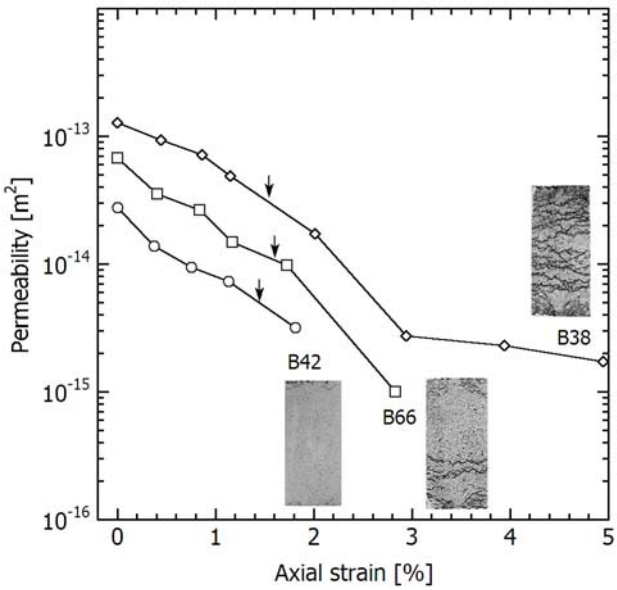


**Figure 3.** Permeability as a function of axial strain during triaxial loading of three samples at an effective pressure of 250 MPa. The arrows mark the onset of shear-enhanced compaction. The microstructure of each sample at the end of the experiment is indicated by the insets with photographs of the thin sections. (Each inset represents axial cross section of a sample.)

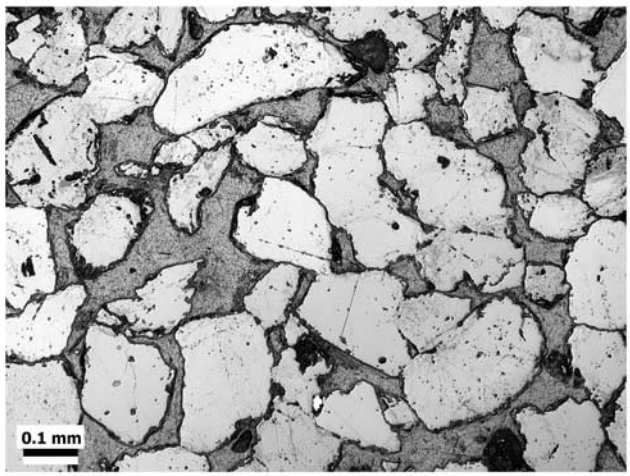


**Figure 4.** Characteristic microstructure of intact Bentheim sandstone (in reflected light). The grains are mostly angular, coated with a thin rim of darker cement. Some of the grain contacts show evidence of pressure solution.

determined from the initial slope of a plot of the differential stress versus axial strain (Figure 1a). These mechanical data are also compiled in Table 2.

## 5. Discussion

[26] In this study we have followed the methodology of *Zhu and Wong* [1997], who conducted an extensive investigation of the evolution of permeability in five sandstones with porosities ranging from 15% to 35%. This previous study has underscored the control of porosity and stress state on permeability, particularly in relation to the onset of dilatancy and shear-enhanced compaction associated with the failure modes involving brittle faulting and compactive cataclastic flow. In the brittle faulting regime, while concomitant development of dilatancy and permeability enhancement is generally observed in sandstones with porosities of 15% or less, the bulk permeability may actually decrease in a highly porous sandstone undergoing dilatancy. Under high confinement, permeability reduction of more than two orders of magnitude may develop during compactive failure by distributed cataclastic flow. To capture this complex coupling with inelastic deformation and failure mode, *Zhu and Wong* [1997] proposed a deformation-permeability map as a conceptual model for the different regimes of permeability evolution.

[27] Since Bentheim sandstone has a porosity that falls in the range investigated by *Zhu and Wong* [1997], it is expected that certain aspects of our data are in basic agreement with their conceptual model, especially for dilatant fracture under low confinement and delocalized cataclastic flow under high confinement. Here we will briefly review these similarities, but the discussion will emphasize hydromechanical phenomena associated with the development of compaction or shear localization, that have not been elucidated in the previous study. Indeed, that is the focus of the present study, and our synthesis of the hydromechanical data and microstructural observations reveals additional details on permeability evolution during localized deformation.

### 5.1. Shear Localization and Permeability Evolution

[28] Two of our Bentheim sandstone samples (at effective pressures of 10 and 30 MPa) failed by shear localization (Figure 1a). Permeability in both samples decreased with increasing strain (Figure 2a). However, porosity evolved differently in that while appreciable dilatancy was observed in the sample deformed at effective pressure of 10 MPa (with the implication that permeability and porosity changes were negatively correlated), negligible porosity change was detected in the sample at 30 MPa (Figure 1b). As illustrated in Figure 8a, the permeability and porosity changes in the 10 MPa sample were positively correlated during hydrostatic and triaxial loading up to the onset of dilatancy $C'$, beyond which the correlation changed sign to become negative. As pointed out by *Zhu and Wong* [1997], such a permeability evolution is generally observed in sandstone samples with

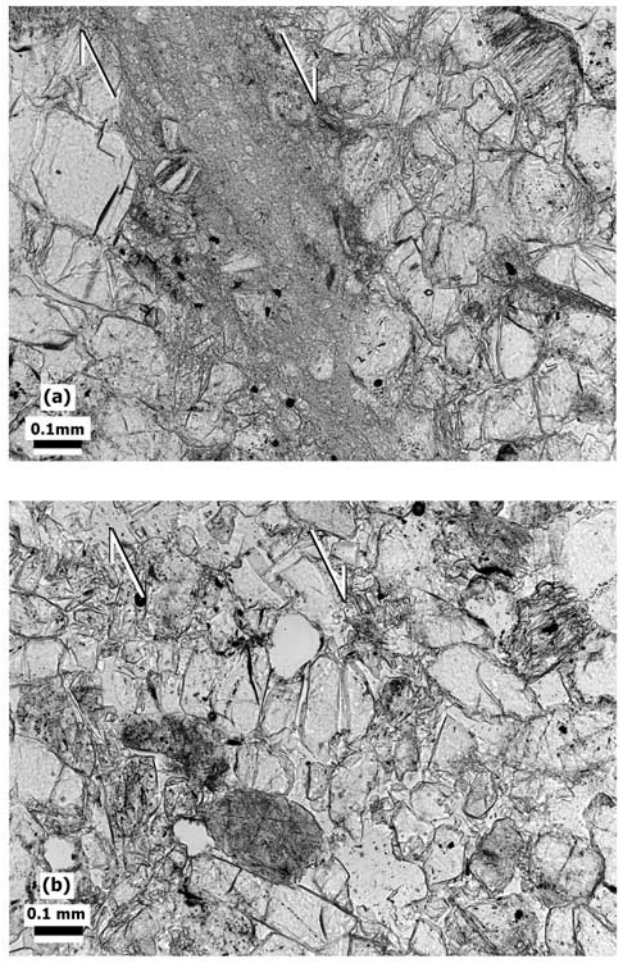


**Figure 5.** Shear localization during triaxial loading at effective pressure of 10 MPa: (a) shear zone characterized by a grain size reduction and a sharp transition to the surrounding damage zone; (b) apparent dilatancy and moderate grain size reduction in the vicinity of an intersection of conjugate shear zones. (Sample B41, plane-polarized light).

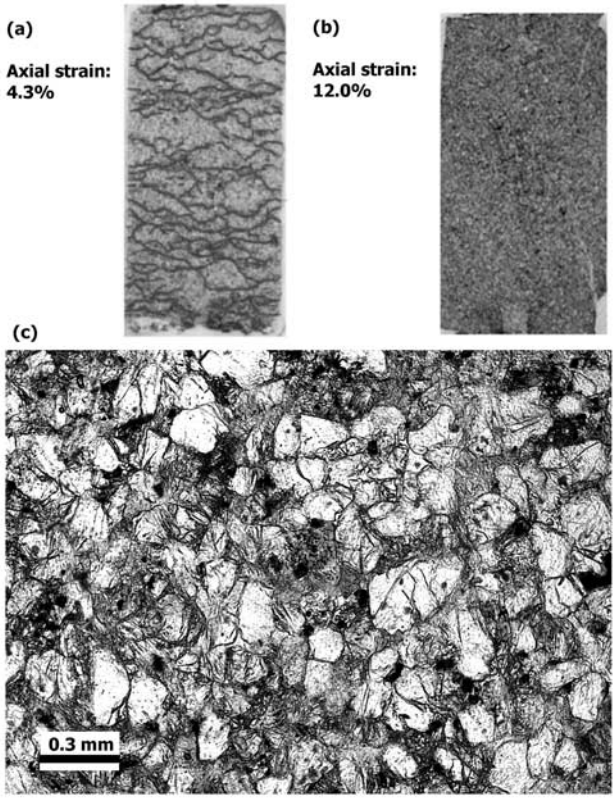


**Figure 6.** Spatial distribution of compaction in samples deformed to a large axial strain at an effective pressure of 300 MPa: (a) discrete compaction bands in a sample loaded to axial strain of 4.3% (B16) (b) high density of compaction bands at axial strain of 12.0% (B33) resembling homogeneous deformation; (c) detail of the central part of Figure 6b showing islands of undamaged grains enclosed by regions of comminuted grains. (Figures 6a and 6b are photographs of thin sections, with a real size of 18 × 38 mm; Figure 6c is a plane-polarized light microscopy.)

initial porosities greater than 15% that fail by dilatant faulting. Recent data of *Heiland and Raab* [2001] as well as our data corroborate this conclusion. To characterize the relative change of permeability from the onset of dilatancy $C'$ to peak stress, *Zhu and Wong* [1997] introduced a pre-failure permeability change parameter $\xi = [k(\text{peak stress}) - k(C')]/k(C')$. For Bentheim sandstone $\xi = -0.3$ and as shown in Figure 8b this negative correlation between permeability and porosity changes is consistent with the trend for other geomaterials compiled by *Wong and Zhu* [1999].

[29] That permeability decrease in a dilatant rock can be attributed to the complex interplay of pre-existing equant pores and stress-induced microcracks that perturbs simultaneously the pore size distribution and connectivity, was captured in a network model developed by *Zhu and Wong* [1996] and applied to Berea sandstone. Since geometric attributes of the pore space in the Bentheim sandstone samples are qualitatively similar to those in Berea sandstone [*Menéndez et al.*, 1996], it is likely that a similar network model would apply here. However, it should also be noted that such a model applies only to delocalized deformation that occurs from the onset of dilatancy to that point in the post-peak stage when shear localization initiates. With the inception of strain localization, it is necessary to model the failed sample as a heterogeneous structure with increasing number of deformation bands [*Main et al.*, 2000].

### 5.2. Permeability Evolution With Porosity Reduction During Compactive Failure

[30] In all our samples that underwent shear-enhanced compaction and strain hardening, there was a consistent trend for permeability to decrease with porosity reduction. In agreement with the deformation-permeability map of *Zhu and Wong* [1997], a significant drop in permeability of more than one order of magnitude was observed with the onset of shear-enhanced compaction (Figure 2b). In these samples, permeability as a function of porosity apparently evolves along three separate regimes with distinctly different slopes, marked as I, II and III in Figure 9. Regime I corresponds to the hydrostatic loading followed by triaxial loading up to the onset of shear-enhanced compaction $C^*$. For hydrostatic loading *David et al.* [1994] compiled data of permeability $k$ as a function of porosity $\phi$ in sandstones with porosities ranging between 14% and 35%, and when fitted to a power law of the form $k \propto \phi^{\alpha}$ they obtained values of the exponent $\alpha$ between 4.6 and 25.4. In agreement with this observation, our Bentheim sandstone data in regime I can be fitted to a power law with $\alpha = 21.9$, comparable to that for the more porous sandstones analyzed by *David et al.* [1994].

[31] The onset of compactive yield is manifested by shear-enhanced compaction, with permeability decreasing rapidly with porosity reduction in regime II. Subsequently the permeability evolution becomes more gradual in regime III. While such distinct signatures of permeability evolution may imply apparently different mechanisms, this interpretation is subject to the assumption that the strain and

**Table 2.** Mechanical and Microstructural Data Used in Quantification of the Relation Between Plastic Strain and the Number of Discrete Compaction Bands

| Sample | $P_c - P_p$, MPa | Pore Fluid | $\varepsilon_{ax}$, % | $Q$, MPa | $\varepsilon^*$, % | $Q^*$, MPa | $E$, GPa | $\varepsilon_p$, % | $n$ | Reference |
|---|---|---|---|---|---|---|---|---|---|---|
| B6 | 180.0 | air | 4.41 | 252.9 | 1.16 | 230.2 | 21.6 | 3.15 | 13 | *Wong et al.* [2001] |
| B9 | 300.0 | air | 3.21 | 221.0 | 0.98 | 181.6 | 21.5 | 2.05 | 11 | *Wong et al.* [2001] |
| B11 | 120.0 | air | 3.78 | 236.0 | 1.35 | 243.0 | 19.2 | 2.47 | 11 | *Wong et al.* [2001] |
| B12 | 300.0 | air | 1.40 | 170.2 | 0.80 | 170.2 | 22.3 | 0.59 | 3 | *Baud et al.* [2004] |
| B16[a] | 300.0 | water | 4.32 | 209.0 | 0.98 | 170.1 | 19.0 | 3.14 | 22 | this study |
| B20 | 300.0 | air | 5.79 | 187.7 | 0.78 | 125.8 | 16.6 | 4.64 | 25 | *Baud et al.* [2004] |
| B22 | 300.0 | air | 4.06 | 180.6 | 0.88 | 164.9 | 21.7 | 3.10 | 19 | *Baud et al.* [2004] |
| B38 | 250.0 | water | 4.95 | 205.1 | 1.55 | 226.6 | 15.8 | 3.54 | 11 | this study |
| B42 | 250.0 | water | 1.81 | 194.9 | 1.46 | 217.1 | 16.8 | 0.48 | 0 | this study |
| B66 | 250.0 | water | 2.83 | 192.2 | 1.60 | 224.7 | 15.9 | 1.43 | 2 | this study |

[a]Continuous loading; no permeability measurements.

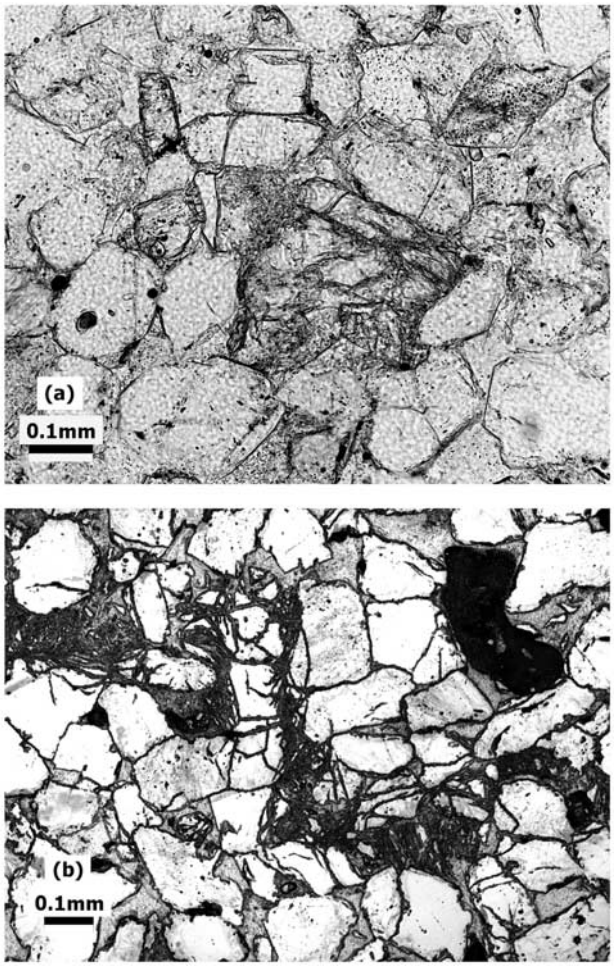


**Figure 7.** Evolution of compaction localization during triaxial loading at an effective pressure of 250 MPa: (a) an isolated cluster of crushed grains in a sample loaded just beyond the onset of shear-enhanced compaction (B42, plane-polarized light); (b) a tortuous compaction band in a sample loaded significantly past the onset of shear-enhanced compaction (B66, reflected light).

porosity distributions in the failed sample are relatively homogenous. In light of our microstructural observations (Figures 6 and 7) as well as those of *Wong et al.* [2001] and *Baud et al.* [2004] that clearly show the onset of compaction localization during regime II, it is questionable whether global measures of deformation such as strain and porosity can realistically reflect the complex heterogeneous deformation in the sample. A more comprehensive interpretation of the permeability evolution in regimes II and III hinges on understanding the development of compaction localization and its consequence on hydraulic flow that are studied in the two following sections.

### 5.3. Number of Compaction Bands as a Function of Plastic Strain

[32] The data compiled in Table 2 indicate that there is an overall trend for the number $n$ of compaction bands to increase linearly with accumulation of plastic strain $\varepsilon_p$ (Figure 10). Since the data are from ten experiments on dry or saturated samples deformed at different effective pressures, there is significant scatter. No systematic dependence on either pressure or saturation conditions was detected. The data can be fitted to the relation

$$\varepsilon_p = \varepsilon_0 + \beta \cdot n, \tag{1}$$

with coefficients $\varepsilon_0 = 4.02 \times 10^{-3}$ and $\beta = 1.76 \times 10^{-3}$ determined by linear regression. That the coefficient $\varepsilon_0$ is positive implies that with the onset of shear-enhanced compaction $C^*$ this amount of inelastic strain had to first

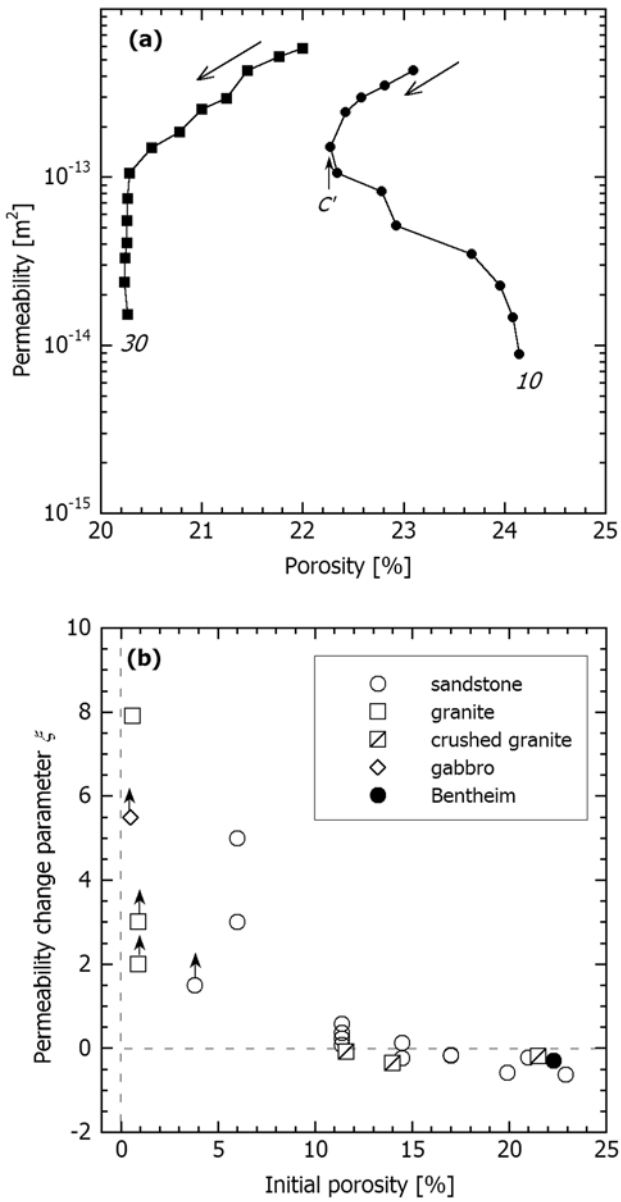


**Figure 8.** Permeability evolution during shear localization. (a) Permeability as a function of porosity. The long arrows indicate the progress of the experiments. The short arrow marks the onset of shear-induced dilatancy. Effective pressures are indicated for each experiment. (b) Comparison of the prefailure permeability change parameter $\xi$ of Bentheim sandstone, with geomaterials compiled by *Wong and Zhu* [1999].

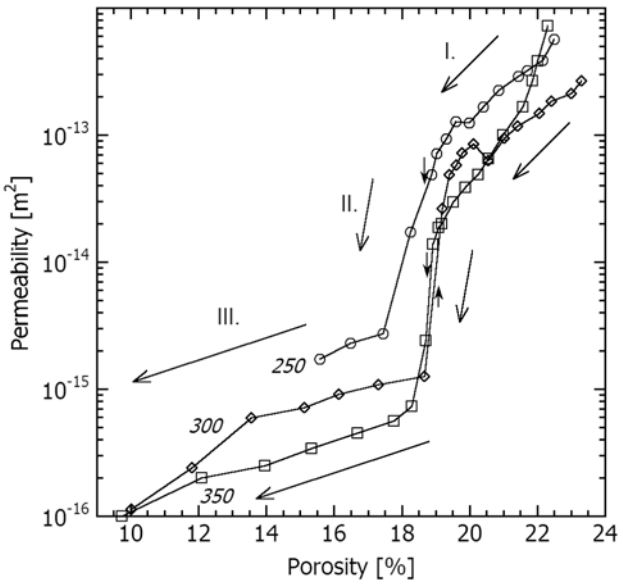


**Figure 9.** Permeability evolution as a function of porosity during compaction localization. Numbers I, II, and III and the long arrows indicate the progress of the experiments and refer to three different regimes in the permeability-porosity evolution. The small solid arrows mark the onset of shear-enhanced compaction. Effective pressures are indicated for each experiment.

develop before compaction band formation initiated. The stress state that corresponds to this point (with $n = 0$ and $\varepsilon_p = \varepsilon_0$) is denoted by $C_{cb}$ in Figure 2a. In the above analysis it is implicitly assumed that effects of effective pressure from 120 to 300 MPa and saturation on the cumulative development of compaction bands would be small compared with the sample-to-sample variability.

[33] The linear relation equation (1) implies that addition of each compaction band is associated with about the same amount of plastic strain $\varepsilon_p = \beta$. According to the microstructural interpretation of *Baud et al.* [2004], once compaction bands have initiated the inelastic deformation is primarily taken up by localized damage within the bands, which in Bentheim sandstone have widths on the order of $l \sim 0.5$ mm (between 2 and 3 grains). Our estimate of the strain $\beta = 1.76 \times 10^{-3}$ represents a shortening of $\Delta l = 0.07$ mm normalized to the total sample length 38 mm. If indeed this inelastic shortening is all taken up by damage localized in a single band of width $l$, then the localized strain is given by $\beta' = \Delta l/l = 0.14$ which presumably corresponds to localized reduction of porosity by 14% (neglecting the lateral deformation). This estimate is comparable to the value of 15% that *Baud et al.* [2004] inferred independently from the duration of acoustic emission activity associated with the formation of a single compaction band.

### 5.4. Compaction Localization and Fluid Flow: Effective Permeability of a Medium Embedded With Discrete Layers of Compaction Bands

[34] Development of such intense damage within a compaction band is expected to significantly reduce the pore size and pore connectivity, which can collectively lower the permeability. Motivated by the microstructural observations, we model the failed sample as a layered medium, with discrete layers (of uniform permeability $k_{cb}$ and width $l$) embedded in a matrix (of permeability $k_m \gg k_{cb}$). If there are $n$ such layers embedded within an effective medium of total thickness $L$, then conservation of mass for steady-state flow across the layered medium requires [e.g., *Freeze and Cherry*, 1979] that the effective permeability

$$k_{\text{eff}} = \frac{k_m}{\left(\frac{nl}{L}\right)\left(\frac{k_m}{k_{cb}} - 1\right) + 1} = \frac{k_m}{\left(\frac{\varepsilon_p - \varepsilon_0}{\beta'}\right)\left(\frac{k_m}{k_{cb}} - 1\right) + 1}. \quad (2)$$

[35] According to this model, the permeability evolution with plastic strain depends solely on the ratio $k_m/k_{cb}$, if microstructural data are available to constrain the parameters $\beta' = \beta L/l$ and $\varepsilon_0$. Strictly speaking $k_m$ is given by the permeability at $C_{cb}$ when the compaction band formation has just initiated (with $\varepsilon_p = \varepsilon_0$ and $n = 0$). However, realistically the measurements are often made either before or after this point. At effective pressures of 250 and 300 MPa, we estimated $k_m$ by the data point taken just before $C_{cb}$ (which also coincides with the data point just before $C^*$). However, we do not have microstructural data (such as in Figure 10) on the accumulation of bands in the sample deformed at 350 MPa and therefore we cannot pinpoint $C_{cb}$. For this experiment we consider two possible estimates of $k_m$ that correspond to our data points just before $C_{cb}$ and before $C^*$ (Figure 2a). It can be seen in Figure 11 that the permeability data normalized by $k_m$ for our three experiments can be bracketed by two curves according to equation (2) with $k_m/k_{cb} = 20$ and 400. The rather large range arises from the estimation of $k_m$ for the

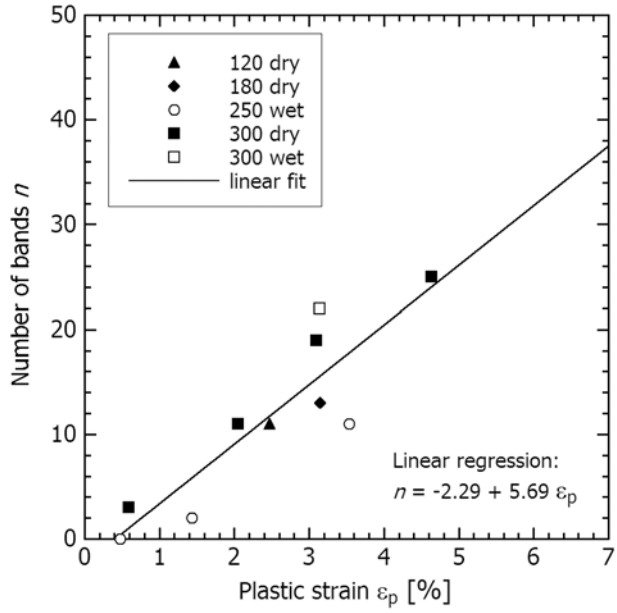


**Figure 10.** Number of compaction bands as a function of axial plastic strain for Bentheim sandstone deformed under various experimental conditions (data from Table 2). The equation represents the linear fit through all data.

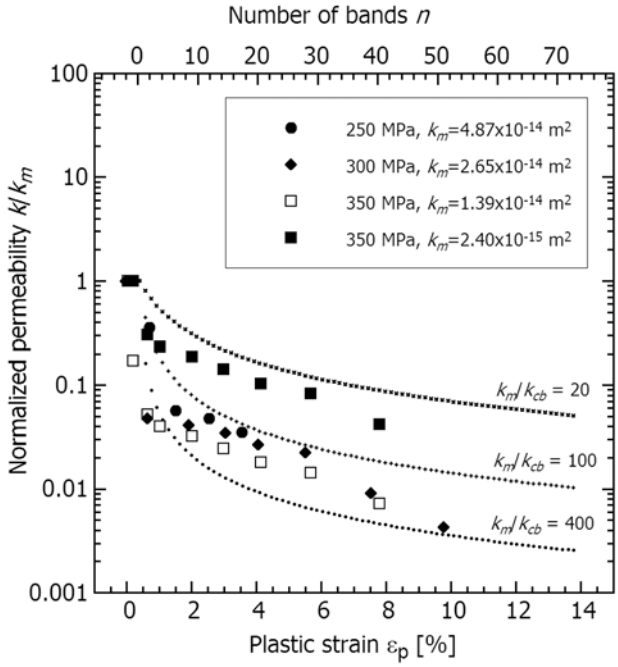


**Figure 11.** Normalized permeability as a function of plastic strain. Data points beyond the onset of shear-enhanced compaction are plotted for experiments at effective pressures of 250, 300, and 350 MPa normalized by value $k_m$ indicated in the figure. The dotted lines represent prediction of equation (2), with the permeability contrast $k_m/k_{cb}$ indicated.

experiment at 350 MPa. The data for effective pressure 250 and 300 MPa fall in a much narrower range bracketed by $k_m/k_{cb}$ = 100 and 400.

[36] In agreement with the experimental observation, the percolative behavior of such a layered medium is initially characterized by permeability reduction of one order of magnitude (corresponding to regime II indicated in Figure 9) that occurs with the development of relatively few (<10) compaction bands. Further development of additional bands decreases the permeability in a more gradual manner (corresponding to regime III in Figure 9). The limiting value of $k_{cb}$ is attained when $nl = L$ (or when $n$ = 76 in our sample).

[37] It can also be seen from equation (2) that according to this model, the permeability evolution with strain is sensitively dependent on $\gamma = (k_m/k_{cb} - 1)/\beta'$. A high value of $\gamma$ implies a relatively rapid drop in permeability as a function of strain. While $(k_m/k_{cb} - 1)$ characterizes the relative permeability reduction in the compaction band, the parameter $\beta'$ $(= \Delta l/l)$ reflects the localized damage and pore collapse. Hence the parameter $\gamma$ can be considered as a measure of how effective pore collapse can reduce the permeability and in this sense it is analogous to the exponent $\alpha$ discussed in section 5.2.

### 5.5. Permeability Evolution in Discrete Versus Diffuse Compaction Bands

[38] There are still many unanswered questions on why compaction bands have widths that vary significantly between the discrete and diffuse end-members, and how to scale the laboratory data to field settings [*Rudnicki*, 2002; *Baud et al.*, 2004]. Nevertheless, our data can provide useful insights in to the hydraulic behavior related to these phenomena. Are the developments of discrete and diffuse compaction bands manifested by different permeability evolutions? In Figure 12 we compare the permeability evolution in a sample of Bentheim sandstone compacted at effective pressure 300 MPa with two samples of Berea sandstone compacted by *Zhu and Wong* [1997] at effective pressures of 160 and 250 MPa. Microstructural observations of *Menéndez et al.* [1996] and recently by *Baud et al.* [2004] concluded that the sample at 160 MPa failed by development of a mosaic of diffuse compaction bands (with width of about 4 grains), while the sample at 250 MPa showed an evidence of delocalized cataclastic flow. The permeability evolution of both Berea sandstone samples show features similar to regimes II and III (Figure 9), as recently analyzed in the constitutive model of *Morris et al.* [2003] for permeability evolution. In regime II the significant permeability reduction occurs over axial strain of about 2% in both samples of Berea sandstone, but somewhat sharper permeability reduction (larger permeability drop over the same amount of axial strain) is observed in the sample deformed at effective pressure of 160 MPa. This apparent difference is possibly due to the development of diffuse compaction bands in the latter sample.

[39] It is of interest to note that the decrease in permeability in Castlegate sandstone that failed by development of diffuse compaction bands occurred over an axial strain of

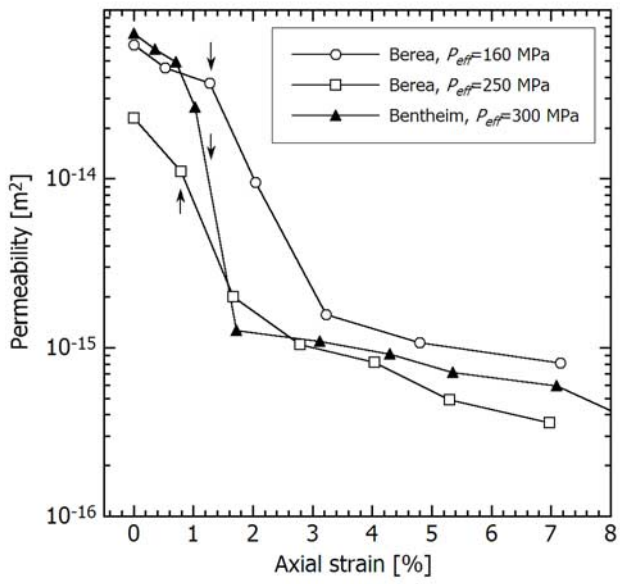


**Figure 12.** Permeability as a function of axial strain in Bentheim (solid symbols) and Berea (open symbols, data from *Zhu and Wong* [1997]) sandstone. The three regimes of permeability reduction can be recognized in both sandstones. Regime II is more gradual in Berea sandstone, where diffuse compaction bands develop, than that in Bentheim sandstone, where discrete compaction bands develop. The arrows mark the onset of shear-enhanced compaction.

~2% [*Holcomb and Olsson*, 2003]. Although the amount of permeability drop was larger than in Berea and Bentheim sandstones, the overall permeability evolution in both Berea and Castlegate sandstones still seems to be more gradual then that in the Bentheim sandstone, where permeability drop occurred over axial strain of less than 1% (Figure 2a). To receive the same amount of permeability reduction, larger strain has to be accumulated in material deforming by diffuse compaction bands. Such observations are not represented by the parameters of the layered medium model and unfortunately, this seems to be the limitation of the model. It should also be noted that the simple model here assumes the bands are planar with uniform width, thus neglecting the possible effects of variable width and tortuosity on the effective permeability. It is also assumed that the permeability contrast of the bands and the matrix remains constant neglecting any distributed deformation within the matrix, which may be an important factor especially in rocks deforming by diffuse compaction bands.

[40] While these tentative conclusions can only be reinforced by more systematic laboratory measurements and microstructural analyses for different sandstones, they have important implications on fluid flow in clastic sedimentary formations. When such a formation undergoes mechanical compaction, the permeability and its anisotropy are sensitively dependent on strain localization. For the same amount of average strain applied to a formation, the most significant permeability reduction (for flow parallel to the maximum principal stress) would develop if localized failure develops in the form of discrete compaction bands. Conversely, the least reduction is expected if the deformation is delocalized. Permeability evolution falls between these two end-members if the deformation is localized in diffuse compaction bands. Of course, these differences disappear under very high strain when damage is pervasive throughout the formation and the effective permeability for the three structural configurations would converge.

[41] A similar scheme may also apply to a formation that fails by shear localization with the development of intersecting deformation bands if the geometric complexity is accounted for [*Caine et al.*, 1996].

[42] We do not have laboratory measurements for the effective permeability parallel to the compaction bands. However it is expected from the overall behavior of a layered model [*Freeze and Cherry*, 1979] that the discrete compaction bands will induce the strongest anisotropy in permeability, with effective permeability in $\sigma_2$ and $\sigma_3$ directions significantly higher than that in $\sigma_1$ direction. Our laboratory study has identified some of the important damage mechanics and geometrical attributes, and in conjunction with current field studies of compaction bands [e.g., *Sternlof and Pollard*, 2002] and numerical analyses [*Sternlof et al.*, 2004], it will provide useful insights for a more comprehensive understanding of the coupling of compaction localization and fluid flow.

## 6. Summary

[43] To investigate the coupling between strain localization and permeability we conducted triaxial compression experiments at effective pressures from 10 to 350 MPa with in situ permeability measurements and microstructural observations of failed samples on Bentheim sandstone. Two types of localized failure were observed: shear localization at effective pressures of 10 and 30 MPa, and compaction localization at effective pressures of 120, 250, 300 and 350 MPa. In both failure modes the permeability decreased with increasing deformation, with the more significant drops observed during compaction localization.

[44] From the onset of dilatancy to shear localization, permeability and porosity changes were negatively correlated in agreement with *Zhu and Wong*'s [1997] conclusion for sandstone samples with initial porosities greater than 15%. During compaction localization, the permeability-porosity evolution is characterized by three regimes. The initial moderate decrease evolves into relatively rapid drop at the onset of shear-enhanced compaction followed again by a more moderate decrease. As compaction localization develops, global measures of deformation such as strain and porosity cannot realistically reflect the complex deformation in the sample. To achieve a more comprehensive understanding of the hydromechanical behavior we quantified the spatial distribution of damage and compaction bands as a function of axial plastic strain. An overall trend was found for the number of discrete compaction bands to increase linearly with accumulation of plastic strain.

[45] Motivated by the microstructural observations, we modeled the failed sample as a layered medium, with discrete layers of uniform thickness with relatively low permeability $k_{cb}$ embedded in a matrix with high permeability $k_m$. According to this model the permeability evolution is governed by parameter $\gamma$ that depends on the permeability contrast ($k_m/k_{cb} - 1$) between the matrix and compaction bands as well as on the localized damage $\beta'$ in the band.

[46] Comparison with laboratory data on Berea and Castlegate sandstones, which developed diffuse compaction bands, indicate that the permeability evolution with strain is more gradual than that in Bentheim sandstone which developed discrete compaction bands. This difference in permeability evolution with strain could be possibly attributed to the higher connectivity of pore space in diffuse compaction bands and as one reviewer (K. Mair) suggested also by distinct way of accommodation the damage outside the diffuse compaction bands. Our results imply that permeability and its anisotropy are sensitively dependent on strain localization. For the same amount of average strain applied to a formation, the most significant permeability reduction (for flow perpendicular to the maximum principal stress) and anisotropy would develop if localized failure develops in the form of discrete compaction bands. Conversely, the least reduction is expected if the deformation is delocalized.

[47] **Acknowledgments.** Wenlu Zhu provided important input into many aspects of this study. We have benefited from discussions with her as well as with Joanne Fredrich, Bill Olsson, John Rudnicki, and Kurt Sternlof. We are grateful to the three reviewers, Dan Faulkner, Karen Mair, and John Rudnicki, for their critical comments and suggestions of improvements. This research was partially supported by the Office of Basic Energy Sciences, Department of Energy under grant DE-FG02-99ER14996.

## References

Antonellini, M., and A. Aydin (1994), Effect of faulting on fluid flow in porous sandstones: Petrophysical properties, *AAPG Bull.*, *78*, 355–377.

Baud, P., W. Zhu, and T.-f. Wong (2000), Failure mode and weakening effect of water on sandstone, *J. Geophys. Res.*, *105*, 16,371–16,389.

Baud, P., E. Klein, and T.-f. Wong (2004), Compaction localization in porous sandstones: Spatial evolution of damage and acoustic emission activity, *J. Struct. Geol.*, *126*, 603–624.

Borja, R. I., and A. Aydin (2004), Computational modeling of deformation bands in granular media, I. Geological and mathematical framework, *Comput. Methods Appl. Mech. Eng.*, *193*, 2667–2698.

Bouteca, M. J., J.-P. Sarda, and O. Vincke (2000), Constitutive law for permeability evolution of sandstone during depletion, paper 58717 presented at the International Symposium on Formation Damage Control, Soc. of Pet. Eng., Lafayette, La.

Caine, J. S., J. P. Evans, and C. B. Forster (1996), Fault zone architecture and permeability structure, *Geology*, *24*, 1025–1028.

David, C., T.-f. Wong, W. Zhu, and J. Zhang (1994), Laboratory measurement of compaction-induced permeability change in porous rocks: Implication for the generation and maintenance of pore pressure excess in the crust, *Pure Appl. Geophys.*, *143*, 425–456.

DiGiovanni, A. A., J. T. Fredrich, D. J. Holcomb, and W. A. Olsson (2000), Micromechanics of compaction in an analogue reservoir sandstone, in *Proceedings of the 4th North American Rock Mechanics Symposium*, pp. 1153–1160, Am. Rock Mech. Assoc., Seattle, Wash.

Fischer, G. J., and M. S. Paterson (1992), Measurement of permeability and storage capacity in rocks during deformation at high temperature and pressure, in *Fault Mechanics and Transport Properties of Rocks*, edited by B. Evans and T.-f. Wong, pp. 213–252, Academic, San Diego, Calif.

Freeze, R. A., and J. A. Cherry (1979), *Groundwater*, Prentice-Hall, Old Tappan, N. J.

Grueschow, E., O. Kwon, and I. G. Main (2003), Observation and modeling of the suction pump effect during rapid dilatant slip, *Geophys. Res. Lett.*, *30*(5), 1226, doi:10.1029/2002GL015905.

Heffer, K. (2002), Geomechanical influences in water injection projects: An overview, *Oil Gas Sci. Technol. Rev. IFP*, *57*, 415–422.

Heiland, J., and S. Raab (2001), Experimental investigation of the influence of differential stress on permeability of a lower permian (Rotliegend) sandstone deformed in the brittle deformation field, *Phys. Chem. Earth A*, *26*, 33–38.

Holcomb, D. J., and W. A. Olsson (2003), Compaction localization and fluid flow, *J. Geophys. Res.*, *108*(B6), 2290, doi:10.1029/2001JB000813.

Issen, K. A., and J. W. Rudnicki (2000), Conditions for compaction bands in porous rock, *J. Geophys. Res.*, *105*, 21,529–21,536.

Issen, K. A., and J. W. Rudnicki (2001), Theory of compaction bands in porous rock, *Phys. Chem. Earth A*, *26*, 95–100.

Keaney, G. M. J., P. G. Meredith, and S. A. F. Murrell (1998), Laboratory study of permeability in a "tight" sandstone under non-hydrostatic stress conditions, paper 47265 presented at SPE/ISRM Eurock'98, Soc. of Pet. Eng., Trondheim, Norway.

Klein, E., and T. Reuschlé (2003), A model for the mechanical behaviour of Bentheim sandstone in the brittle regime, *Pure Appl. Geophys.*, *160*, 833–849.

Klein, E., P. Baud, T. Reuschlé, and T.-f. Wong (2001), Mechanical behaviour and failure mode of bentheim sandstone under triaxial compression, *Phys. Chem. Earth A*, *26*, 33–38.

Knipe, R. J. (1997), Juxtaposition and seal diagrams to help analyze fault seals in hydrocarbon reservoirs, *AAPG Bull.*, *81*, 187–195.

Louis, L., C. David, and P. Robion (2003), Comparison of the anisotropic behaviour of undeformed sandstones under dry and saturated conditions, *Tectonophysics*, *370*, 193–212.

Main, I. G., O. Kwon, B. T. Ngwenya, and S. C. Elphick (2000), Fault sealing deformation-band growth in porous sandstone, *Geology*, *28*, 1131–1134.

Menéndez, B., W. Zhu, and T.-f. Wong (1996), Micromechanics of brittle faulting and cataclastic flow in Berea sandstone, *J. Struct. Geol.*, *18*, 1–16.

Mollema, P. N., and M. A. Antonellini (1996), Compaction bands: A structural analog for anti-mode I cracks in aeolian sandstone, *Tectonophysics*, *267*, 209–228.

Morris, J. P., I. N. Lomov, and L. A. Glenn (2003), A constitutive model for stress-induced permeability and porosity evolution of Berea sandstone, *J. Geophys. Res.*, *108*(B10), 2485, doi:10.1029/2001JB000463.

Olsson, W. A. (1999), Theoretical and experimental investigation of compaction bands in porous rock, *J. Geophys. Res.*, *104*, 7219–7228.

Olsson, W. A., and D. J. Holcomb (2000), Compaction localization in porous rock, *Geophys. Res. Lett.*, *27*, 3537–3540.

Rudnicki, J. W. (2002), Compaction bands in porous rocks, paper presented at the Proceedings of the International Workshop on Bifurcation and Instability, St. John's Univ., Saint Joseph, Minn, 3–5 June.

Sternlof, K. R., and D. D. Pollard (2002), Numerical modeling of compactive deformation bands as granular "anti-cracks," *83*(47), Fall Meet. Suppl., Abstract T11F-10.

Sternlof, K. R., J. R. Chapin, D. D. Pollard, and L. J. Durlofsky (2004), Permeability effects of deformation band arrays in sandstone, *AAPG Bull.*, *88*, 1–15.

Vajdova, V., and T.-f. Wong (2003), Incremental propagation of discrete compaction bands: Acoustic emission and microstructural observations on circumferentially notched samples of Bentheim sandstone, *Geophys. Res. Lett.*, *30*(14), 1775, doi:10.1029/2003GL017750.

Wong, T.-f. and W. Zhu (1999), Brittle faulting and permeability evolution: Hydromechanical measurement, microstructural observation, and network modeling, in *Faults and Subsurface Fluid Flow in the Shallow Crust*, *Geophys. Monogr. Ser.*, vol. 113, edited by W. Haneberg et al., pp. 83–99, AGU, Washington, D. C.

Wong, T.-f., C. David, and W. Zhu (1997), The transition from brittle faulting to cataclastic flow in porous sandstones: Mechanical deformation, *J. Geophys. Res.*, *102*, 3009–3025.

Wong, T.-f., P. Baud, and E. Klein (2001), Localized failure modes in a compactant porous rock, *Geophys. Res. Lett.*, *28*, 2521–2524.

Zhu, W., and T.-f. Wong (1996), Permeability reduction in a dilating rock: Network modeling of damage and tortuosity, *Geophys. Res. Lett.*, *23*, 3099–3102.

Zhu, W., and T.-f. Wong (1997), The transition from brittle faulting to cataclastic flow in porous sandstones: Permeability evolution, *J. Geophys. Res.*, *102*, 3027–3041.

Zoback, M. D., and J. D. Byerlee (1975), The effect of microcrack dilatancy on the permeability of Westerly granite, *J. Geophys. Res.*, *80*, 752–755.

P. Baud, Institut de Physique du Globe, Ecole et Observatoire des Sciences de la Terre (CNRS/ULP), 5 rue Descartes, F-67084 Strasbourg, France. (pbaud@eost.u-strasbg.fr)

V. Vajdova and T.-f. Wong, Department of Geosciences, State University of New York at Stony Brook, Stony Brook, NY 11794-2100, USA. (vvajdova@ic.sunysb.edu; teng-fong.wong@stonybrook.edu)